

Contents lists available at ScienceDirect

Journal of the Mechanics and Physics of Solids

journal homepage: www.elsevier.com/locate/jmps





Microstructure realization of a lattice-based polar solid for arbitrary elastic waveguiding

Shiheng Zhao a, Jiaji Chen b, Zheng Chang a,*, Guoliang Huang b,*

- ^a College of Science, China Agricultural University, Beijing 100083, China
- ^b Department of Mechanical and Aerospace Engineering, University of Missouri, Columbia, MO 65211, USA

ARTICLE INFO

Keywords: Transformation elasticity Waveguide Lattice-based polar solid Rayleigh wave

ABSTRACT

The ability to precisely directing and controlling longitudinal (P) and transverse (S) waves in 2D solids along an arbitrary trajectory has attracted significant research interest and is crucial for practical applications such as imaging, cloaking, and wave focusing. Here, we report, design and examine an inhomogeneous lattice-based polar medium for ideal elastic waveguide, whose microstructures are inversely determined by the discrete transformation elasticity (DTE). Microstructures of the suggested medium, which are realized through global linear transformation and local affine transformation, enables arbitrary waveguides to transport elastic waves with minimal energy loss. Numerical simulation is then conducted to demonstrate that the lattice-based polar waveguide can efficiently steer both in-plane P and S wave modes over a broad frequency band. We also leverage the medium for Rayleigh wave control on curved surfaces. The constructed polar surface can break the conventional limit of the Rayleigh wave propagation on both concave and convex surfaces with extreme curvatures. This study is not only a concrete manifestation of the polar material, discrete transform elasticity, and their advantages but also provides a great potential in engineering applications such as signal detection, vibration control, and earthquake protection.

0. Introduction

Being an outstanding example of wave steering, wave cloaking refers to wave being bent in a precise fashion to prevent it from being scattered by the cloaked object. Since the very first realization of cloak device by Pendry and his colleagues (Pendry et al., 2006), wave cloaking attracts tremendous research interests due to its great potential in steal technology, vibration mitigation, imaging and energy harvesting, etc (Bückmann et al., 2015; Chang et al., 2014a, 2011; Gokhale et al., 2012; Meirbekova and Brun, 2020). The transformation method provides the ultimate tool for designing cloak device for systems governed by form-invariant equations under a curvilinear change of coordinates, for instance, thermal conductivity equations (Chang et al., 2014b; Kadic et al., 2015; Schittny et al., 2013), acoustic wave equations (Cummer and Schurig, 2007; Norris, 2008; Zhang et al., 2011) and Maxwell's equations of electromagnetism (Chen et al., 2010; Schurig et al., 2006). Researchers have achieved great advancement in experiment and manufacture in these domains. However, there is little to no progress in transformed material (metamaterials derived from the transformation method) for elastic wave control. Due to the stringent requirements imposed by the transformation method on material properties, this topic can be considered the most challenging one in the field of metamaterials. The major obstacle is that the corresponding Navier's equation is not form-invariant under the transformation method (Chang et al., 2015; Norris and Parnell, 2012; Norris and Shuvalov, 2011). Form-invariance is in its essence a problem in material and its microstructure design.

E-mail addresses: changzh@cau.edu.cn (Z. Chang), huangg@missouri.edu (G. Huang).

^{*} Corresponding authors.

According to the transformation elasticity, the desired elasticity tensor \mathbf{c} of transformed elastic materials are attributed to three factors: (1) the elasticity tensor \mathbf{C} of the background medium before transformation, (2) the gradient $\mathbf{F} = \partial \mathbf{x}/\partial \mathbf{X}$ of a space-warping transformation ϕ , which maps a point \mathbf{X} in a virtual space to another point \mathbf{x} in a real space and defines the geometry of the transformed material, and (3) displacement gauge defined by $\mathbf{u}(\mathbf{x}) = [\mathbf{B}(\mathbf{X})]\mathbf{U}(\mathbf{X})$. For full elasticity, the geometric-constitutive equivalence principle is broken since most geometric transformations yield hypothetical constitutive properties that no known elastic material satisfies. Two well-known categories of hypothetical transformed materials have been reported in previous literatures with two distinct transformations used (Brun et al., 2009; Milton et al., 2006). Under the Milton-Briane-Willis gauge with $\mathbf{B} = \mathbf{F}^T$, the transformed materials support symmetric stresses and a modified Hooke's law coupling stresses to displacements, known as Willis materials (Willis, 1981). Under the Brun-Guenneau-Movchan (BGM) gauge with $\mathbf{B} = \mathbf{I}$, the transformed materials support non-symmetric stresses (i.e., $c_{ijkl} = c_{jikl}$), which are called polar materials (Nassar et al., 2019; Zhang et al., 2020a). However, these state-of-the-art descriptions provide no insight into what the underlying microstructure of this transformed material could be, the design of which remains challenging in this field.

Recently, the microstructures of polar materials under the BGM gauge have been suggested and their application for perfect elastic cloaking has been demonstrated theoretically and experimentally for the gradient F being either conformal or radically symmetric (Chen et al., 2021; Nassar et al., 2020; Xu et al., 2020). The polar material is similar to a Cosserat medium in that they both support non-symmetric stresses, though not necessarily featuring any additional degrees of freedom. Thus, it is best qualified not as a Cosserat medium but as a Cauchy medium with torque induced non-symmetric stress instead of coupled stress. The solid medium is polar in the sense that it resists elastic rotation and is also degenerated, meaning it admits a stressless collapse mechanism. To extend the application of the transformation elasticity under the general gradient F, the discrete transformation elasticity (DTE) (Chen et al., 2021) was developed. DTE unlocks the microstructure design of anisotropic polar medium with chiral properties. The method bridges the spatial equivalence of a continuum and lattice material and provides a systematic procedure for the inverse design of transformed elastic media. As a promising application beyond the elastic cloaking of the polar material, the omnidirectional longitudinal-shear mode conversion and anomalous polarization were investigated (Wu and Huang, 2022). To the best of our knowledge, how to realize microstructures of the polar materials for arbitrary waveguide has never been reported yet. The transformed lattice elements for such purpose would steer elastic waves in a sense that would not strictly follow the homogeneous transformation elasticity approach.

In this study, the lattice-based elastic polar medium is leveraged to realize arbitrary waveguiding in the elastic medium based on the finite embedded coordinate transformation, which is one of the most challenging engineering problems of elastic wave control. We expand the class of inhomogeneous transformation elastic structures by affine transformations that can be designed to device-type structures capable of steering elastic waves. Various transformed media with different waveguiding functionalities will be formulated under global linear and local affine transformation theory with different gradients F and the DTE will be adopted for physically realizing its feasible microstructures. We numerically demonstrate that the proposed waveguides can not only manipulate both in-plane Gaussian beams in P and S modes along the different paths over a broad frequency band, but also overcome the limitation of surface curvature and realize the perfect waveguiding or filtering of Rayleigh waves on concave and convex curved surfaces. It should be emphasized that affine transformations could add a significant flexibility to the transformation design of complex waveguiding, enabling the transfer of the wave field from one transformed elastic medium to another. Therefore, the designed waveguides can be impedance matched and, through deliberate assembly, can perform various functionalities such as unidirectional cloaking and arbitrary waveguiding. Our study provides great potential of using the DTE paradigm to design modern elastic wave control devices.

The remainder of the paper goes as follows: In Section 1, we review the continuum and discrete transformation elasticity for inverse design of the transformed medium under the generalized gradient F; the mechanism of global linear transformation and local affine transformation is also revealed and discussed. The detailed microstructure design and the numerical validation of the lattice-based polar solids are presented for in-plane longitudinal and shear wave steering in Section 2. In Section 3, we theoretically and numerically demonstrate how to break limit of Rayleigh wave propagation on curved surfaces with excessive curvature. Finally, the concluding remarks and a discussion of avenues for future work are given in Section 4.

1. Continuum and discrete transformation elasticity

In this section, we briefly review the elasticity continuum transform under the BGM gauge to establish the theoretical foundation of polar medium. The discrete transformation elasticity (DTE) along with discretization of general Cauchy isotropic medium is then suggested for physical realization of the polar solids targeting extreme wave control, aside from the conventional wave cloaking functionality. Furthermore, a systematical coordinate transformation method based on the lattice-based polar medium is proposed by combining global linear and local affine transformations for an arbitrary transformation mapping.

1.1. Continuum transformation elasticity

The constitutive behavior of the transformed continuum medium under the BGM gauge and its key features are first revisited. Consider a general mapping $\mathbf{x} = \phi(\mathbf{X})$ that transform a reference domain $\{\mathbf{X}\}$ (Fig. 1(a)) into a transformed domain $\{\mathbf{x}\}$ (Fig. 1(b)). It is particularly insightful to illustrate the displacement fields $\mathbf{U}(\mathbf{X})$ and $\mathbf{u}(\mathbf{x})$ as two different but equivalent sets of generalized

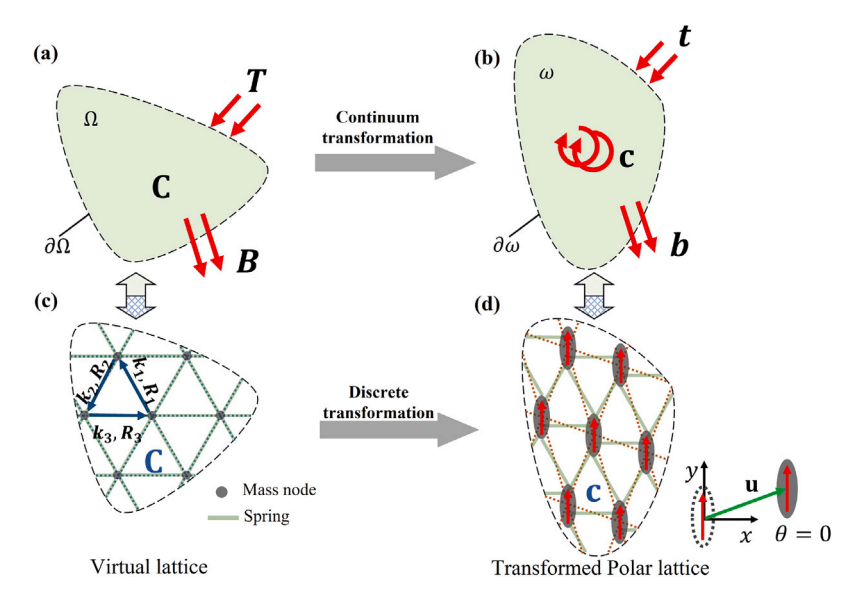


Fig. 1. Schematic representation of the continuum (a-b) and discrete (c-d) transformation. Continuum transformation elasticity under the BGM gauge, an isotropic continuum medium subject to arbitrary boundary and body forces (two straight red arrows) can be transformed into a polar solid (b) with the existence of a body torque. The continuum is elastodynamically equivalent to a discrete lattice (c) within a frequency range. Based on discrete transformation elasticity, the discrete lattice can be transformed into a polar lattice (d) with the rotation of its masses suppressed (inset of (d)).

Lagrangian coordinates. Let $L(\mathbf{E}, \dot{\mathbf{U}})$ and $l(\mathbf{e}, \dot{\mathbf{u}})$ being the Lagrangian densities under the domains $\{\mathbf{X}\}$ and $\{\mathbf{x}\}$, respectively. We have

$$\int_{(\mathbf{X})} L(\mathbf{E}, \dot{\mathbf{U}}) = \int_{(\mathbf{X})} l(\mathbf{e}, \dot{\mathbf{u}})$$
(1)

with $E = \nabla U$, $e = \nabla u$, and \dot{u} being the displacement gradients and velocities under the domains $\{X\}$ and $\{x\}$, respectively. The two energy densities have the coordinate transformation relation

$$L(\mathbf{e}\mathbf{F},\dot{\mathbf{U}})/J = l(\mathbf{e},\dot{\mathbf{u}}) \tag{2}$$

in which $J = \det(\mathbf{F})$ is the determinant of deformation gradient. Let Lagrangian density of an elastic domain $\{\mathbf{X}\}$ be expressed as:

$$L(\mathbf{E}, \dot{\mathbf{U}}) = \frac{\mathbf{E} : \mathbf{C}\mathbf{E} - \dot{\mathbf{U}} \cdot \rho_0 \dot{\mathbf{U}}}{2}$$
(3)

with **C** the elasticity tensor and ρ_0 the mass density. Then, the Lagrangian density in the transformed domain $\{\mathbf{x} = \phi(\mathbf{X})\}$ reads

$$l(\mathbf{e}, \dot{\mathbf{u}}) = \frac{1}{J} L(\mathbf{e}\mathbf{F}, \dot{\mathbf{U}}) = \frac{\mathbf{e} : \mathbf{c}\mathbf{e} - \dot{\mathbf{u}} \cdot \rho_0 \dot{\mathbf{u}}}{2}$$
(4)

and the BGM gauge is adopted by enforcing the equality between original and transformed displacements as $\mathbf{u}(\mathbf{x}) = \mathbf{U}(\mathbf{X})$. The transformed elasticity tensor \mathbf{c} and mass density ρ can be extracted as

$$c_{ijkl} = \frac{F_{jm}F_{ln}C_{imkn}}{I}, \ \rho = \frac{\rho_0}{I}$$
 (5)

Therein, it can be readily checked that **c** does not have the minor symmetries as **C** has, where $C_{ijkl} = C_{jikl} = C_{ijlk}$ does not imply a similar relation for **c**. Consequently, the stress σ that reigns in $\{x\}$ in the presence of a displacement gradient **e** is given by

$$\sigma = \mathbf{ce} \text{ or } \sigma_{ij} = c_{ijkl}e_{kl}$$
 (6)

and is asymmetric in general: $\sigma_{ij} \neq \sigma_{ji}$. The solid is "polar" with the existence of a body torque density linearly dependent over the displacement gradient as $t_i = \epsilon_{ijk}\sigma_{jk} = \epsilon_{ijk}c_{jklm}e_{lm}$, where t is the body torque and ϵ_{ijk} is the permutation symbol, as shown in Fig. 1(b). In the following, we will construct lattice materials which render the set of elastic materials invariant by arbitrary transformations under the BGM gauge to enable elastic waveguiding.

1.2. Elastodynamic equivalence of a continuum and a discrete lattice

Within a certain frequency range, a discrete lattice can be elastodynamically equivalent to a continuum solid, which will serve as the steppingstone for the discrete transformation elasticity (DTE). For simplicity, we consider the original continuum (Fig. 1(a)) to be isotropic and homogeneous. To discrete the continuum with a periodic lattice structure, the lattice must exhibit

O(2) symmetry (Forte and Vianello, 1997) to represent an identical elastic tensor. Without losing generality, we select the triangular honeycomb (Fig. 1(c)) in this symmetry class among other typical structures such as the Kagome lattice, triangular honeycomb, and hexagonal honeycomb (Phani et al., 2006).

The elastic tensor of the homogeneous and isotropic continuum is assumed as

$$C_{ijkl} = \lambda \delta_{ij} \delta_{kl} + \mu(\delta_{ik} \delta_{jl} + \delta_{il} \delta_{jk}) \tag{7}$$

with the mass density being ρ_0 . The elastic energy per unit area is calculated under a macroscopic displacement gradient **E** over the lattice (Nassar et al., 2018). We assume that the mass is rigid and concentrated in a small geometry, thus neglecting its elastic deformation and the torsion that would induce the deformation of the springs. In this fashion, the elastic energy density $W(\mathbf{E})$ of the unit cell can be expressed as the sum of the elastic energies of all the springs k_i , i = 1, 2, 3 (Fig. 1(c)), i.e.

$$W(\mathbf{E}) = \sum_{i=1}^{3} W_i \tag{8}$$

Thereby, the elastic energy of the ith spring in Eq. (8) reads

$$W_i = \frac{k_i}{2V} \langle \mathbf{E}\mathbf{R}_i, \mathbf{D}_i \rangle^2 \tag{9}$$

where $V = \sqrt{3}a^2/2$ and a is the length of the spring, \mathbf{R}_i is the lattice vector, $\langle \cdot, \cdot \rangle$ represents the inner product and $\mathbf{D}_i = \mathbf{R}_i/|\mathbf{R}_i|$ denotes the orientation of the spring. Substituting Eq. (9) into Eq. (8), the effective elastic tensor of the mass–spring lattice can be derived by

$$\tilde{\mathbf{C}} = \frac{\partial^2 W(\mathbf{E})}{\partial \mathbf{E} \partial \mathbf{E}} \tag{10}$$

where

$$\tilde{C}_{ijkl} = \begin{bmatrix} \frac{1}{8\sqrt{3}} (16k_1 + k_2 + k_3) & \frac{\sqrt{3}}{8} (k_2 + k_3) & \frac{1}{8} (-k_2 + k_3) & \frac{1}{8} (-k_2 + k_3) \\ & \frac{3\sqrt{3}}{8} (k_2 + k_3) & \frac{3}{8} (-k_2 + k_3) & \frac{3}{8} (-k_2 + k_3) \\ & \frac{\sqrt{3}}{8} (k_2 + k_3) & \frac{\sqrt{3}}{8} (k_2 + k_3) \\ & & \frac{\sqrt{3}}{8} (k_2 + k_3) \end{bmatrix}$$

$$(11)$$

$$syms$$

To construct the strain energy equivalence, the continuum solid and the discrete lattice material should have identical elastic tensor when subjecting to the same macroscopic displacement. By combining Eq. (7) and (11), we can obtain the constraints on the continuum $\lambda = \mu$, and more importantly, the relationship between the elastic constants of continuum and discrete media as

$$k_1 = k_2 = k_3 = \frac{4}{\sqrt{3}}\mu\tag{12}$$

The equivalent of kinetic energy requires the conservation of mass between the two media, and therefore the relationship between the inertia constants of the two media can be easily obtained as

$$m = \rho_0 V \tag{13}$$

Eqs. (12) and (13) provide a material parameter guideline for the lattice discretization for a continuum from an elastodynamic perspective. We notice that the characteristic length a does not explicitly appear in Eq. (11), indicating that such an equivalent is independent of scale. Nevertheless, from the elastodynamic perspective, the size of the unit cell should be carefully selected to avoid the failure of the equivalence resulting from structural dynamic effects (more related discussion can be found in Section 2). Generally, the lattice constant must satisfy the long-wavelength condition, i.e., it must be several times smaller than the wavelength, meaning that the smaller the unit cell, the wider the frequency band of the discretized structure.

1.3. Discrete transformation theory

DTE (Chen et al., 2021) can be formulated in a similar manner of continuum transformation elasticity in Section 1.1, but from a discrete perspective, which means that the energy of the two domain should still satisfies Eq. (2). Thus, the lattice structure in the transformed domain (Fig. 1(d)), called the transformed lattice, has the elastic energy density in the form of

$$w_i(\mathbf{e}) = \sum_{i=1}^{3} \frac{k_i'}{2v} \langle \mathbf{er}_i, \mathbf{d}_i \rangle^2$$
 (14)

with the spring constants k'_i , the unit cell area v, lattice vector \mathbf{r}_i and spring orientation \mathbf{d}_i . Combining Eqs. (2) (8), (9) and (14) provides the structural relationship of the lattice before and after the transformation as

$$k_i' = k_i \mathbf{d}_i = \mathbf{D}_i$$
 (15)

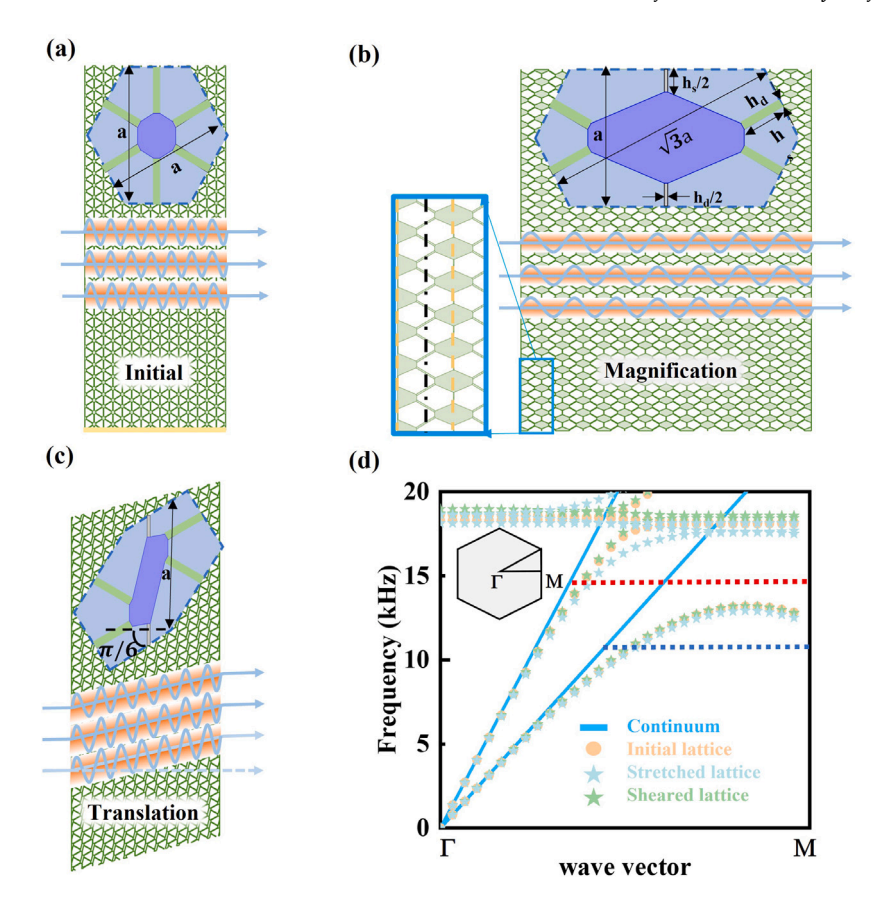


Fig. 2. The design of the polar solids for waveguide with wavelength magnification or beam translation. (a) The initial polar lattice with 15×30 unit cells. The unit cell consists of six identical springs and a dodecagonal mass block. (b, c) The transformed polar lattices for (b) wavelength magnification and (c) beam translation, where the detailed unit cell design is shown in the inset. (d) Dispersion relations of the continuum, the initial and transformed lattices. The irreducible Brillouin zones for the initial lattice are displayed in the inset.

and

$$\mathbf{r}_{i}' = \mathbf{F}\mathbf{R}_{i}$$

$$v = JV$$
(16)

Eq. (15) indicates that the spring constants k_i and the orientations \mathbf{D}_i should be kept the same before and after the transformation, while Eq. (16) suggests that the unit cell area V and lattice vectors \mathbf{R}_i are determined by the Jacobian matrix \mathbf{F} and, generally $\mathbf{r}_i/|\mathbf{r}_i| \neq \mathbf{d}_i$. Correspondingly, the conservation of mass requires the total mass of the transformed region v to be unchanged.

With the positions of the masses and springs of the transformed lattice being determined, it is necessary to adjust the geometry of the mass blocks to form an effective mass–spring connection. Notice that the discrete transformation is constructed by neglecting the torsion and elastic deformation of the mass block. In practice, when the shape and stiffness of the mass blocks cannot satisfy the assumptions, an additional mechanism is required to constrain the rotational degrees of freedom of the mass block. It is also worth noting that such a transformation under the BGM gauge results in the asymmetric stresses. Thus, the transformed lattice should be a polar medium (Chen et al., 2021; Nassar et al., 2018). In summary, the discrete transformation can be easily conducted in the following steps: (1) transform the mass nodes into new locations according to the mapping provided in the spatial transformation, (2) adjust the shapes of springs and masses to ensure interconnection while keeping the stiffness and orientation of the springs together with the magnitude of the masses unchanged, (3) suppress the rotational degrees of freedom of the masses. Square, rectangular, and oblique lattices with anisotropic effective tensors C can be transformed in the same manner.

1.4. Linear and affine transformations for arbitrary waveguiding

By leveraging the spatial transformation gradient **F** in the proposed discrete transformation theory, we can turn wave steering problem into a material design problem accounting for both P and S waves. In general, to realize lattice-based polar microstructures for elastic wave magnification and shifting, the global linear transformation, which is expressed as

$$\mathbf{F} = \begin{bmatrix} \xi_1 & 0 \\ \eta & \xi_2 \end{bmatrix} \tag{17}$$

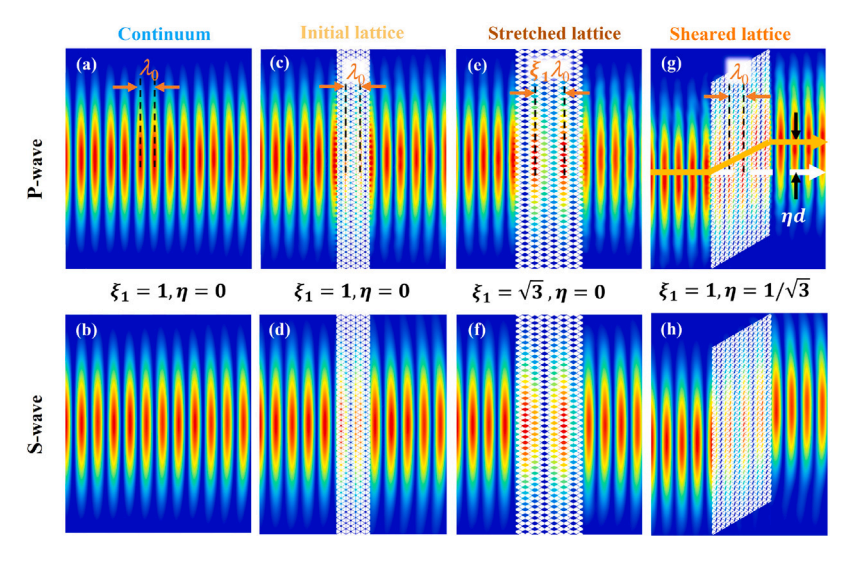


Fig. 3. Numerical simulations for the continuum and the corresponding polar solids. Figures in the first to second row show the results for P wave excited at 13 kHz and S wave excited at 6 kHz, respectively. (a-h) Simulation results of the total displacement field in (a-b) continuum medium, (c-d) initial lattice, (e-f) Stretched lattice and (g-h) sheared lattice.

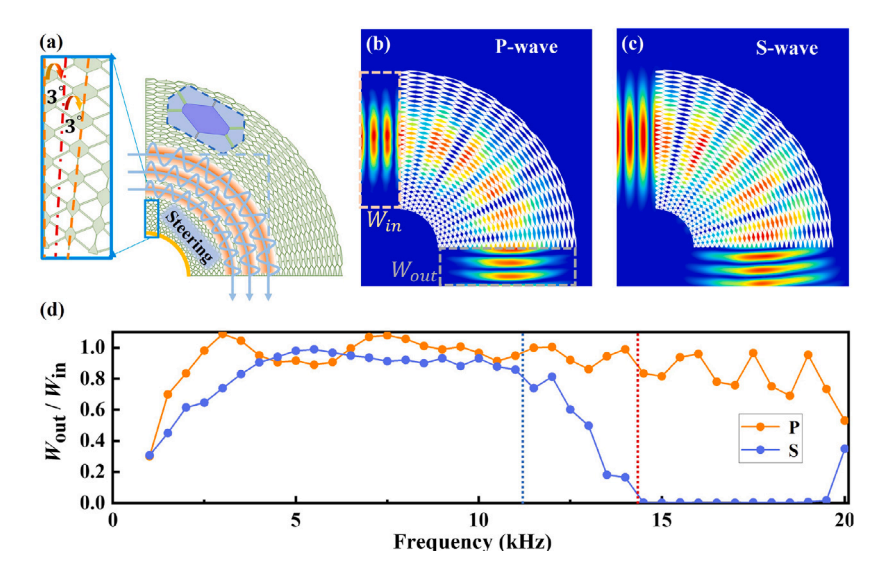


Fig. 4. The design of the polar solid for wave steering. (a) A polar lattice design using local affine transformation. (b-c) Numerical simulation for total displacement fields of the (b) P-wave beam at 12 kHz and (c) the S-wave beam at 6 kHz incident to the polar solid. (d) The transmission spectrum for P- and S-wave beams in the frequency range 1–20 kHz, where W_{in} and W_{out} are the integrals of the deformation energy in the areas identified in (b).

would be applied on an initial domain (Fig. 3(a)) since its corresponding transformation media is homogeneous. In Eq. (17), ξ_1 , ξ_2 and η denote the elongation ratios in X_1 and X_2 directions and tangent of the shear angle, respectively. For simplicity, we confine stretching in the X_2 direction to $\xi_2=1$ to ensure the impedance match between the transformed polar solids and the host medium in the X_1 direction. It is worth noting that different polar solids can be assembled in this direction, which is essential to achieve arbitrary waveguiding. In this context, transformed polar solids for wavelength magnification and beam translation can be obtained by, for examples, making $\xi_1=\sqrt{3}$, $\eta=0$ (uniaxial stretching), and making $\xi_1=1$, $\eta=1/\sqrt{3}$ (simple shear), respectively, as demonstrated in Fig. 2(b,c).

To achieve arbitrary direction or beam steering, an inhomogeneous transformation must be considered. A simple yet feasible solution is to adopt a local affine transformation on the lattice-based medium, i.e., to apply local linear transformations. With assumption of local affine transformation for a mapping, F, the deformation gradient tensor induced by the mapping, can be decomposed as F = VR where R and V denote a rigid rotation and a pure stretch tensor, respectively. Distinguished from R = Const. in above global linear transformations, R varies continuously to map a straight line to a curve, and thereby governs the direction of wave propagation. Along the curve, the infinitesimal elements undergo a series of local affine transformations, i.e., the linear

Table 1
Material parameters for continuum and lattice components (Ashby, 2008).

	Material	Young's Modulus (GPa)	Poisson's ratio	Density (kg/m³)
Continuum	POM (Polyoxymethylene)	1.4	0.33	1350
Spring	PET (Polyester)	15.66	0.33	1800
Mass	Stainless steel	200	0.29	7870

pure stretch mappings as Eq. (17) with $\eta=1$, point by point in the principal coordinate systems. The local form-invariance of the Navier equation ensures a perfect transformation of elastic waves in each infinitesimal element. The approximations made in the connection of adjacent elements indeed undermine global form invariance. Nevertheless, it has already been shown that such those errors stem from approximations can be neglected (Chang et al., 2010; Hu et al., 2011), and wave manipulation with sufficient accuracy is expected.

For example, to bend a rectangular domain (Fig. 2(a)) into an annular circular sector (Fig. 4(a)), the lower boundary of the rectangular (marked in yellow) is continuously bent into a curve as highlighted. The local affine transformation experienced by each infinitesimal element on the curve on the principal coordinate systems has the form of Eq. (17) with $\eta = 1$ (no rigid rotation), $\xi_2 = 1$ (no stretch in the vertical direction of the rectangular), and ξ_1 equals the length ratio of the curve after to the one before the mapping. In this scenario, the local affine transformation gives gradient elements along the radial direction (as shown in inset of Fig. 4(a)), and thus leads to inhomogeneous global mapping.

In short, based on the discrete transformation theory, the arbitrary waveguiding can be constructed in following two steps: First, we perform global linear transformations on the initial lattice-based polar solid to design global wave paths that feature wavelength magnification/compression and beam translation; then, the local affine transform is implemented to locally transform the lattice-based polar structures to meet desired wave-steering capability.

2. Microstructure design and numerical validation

In this section, we would determine the material and structural composition of the initial polar lattice. Moreover, lattice-based polar solids with different waveguiding functionalities would be constructed using global linear and local affine transformations. We would further validate the elastodynamic equivalence between the continuum and lattice-based polar solids and their corresponding wave phenomena by examining their dispersion relations and steady-state wave field.

2.1. Material and structure of the initial polar solid

We consider a rectangular domain made of POM (Polyoxymethylene, Table 1), and discretize it into a mass–spring lattice consisting of 15×30 unit cells (Fig. 2(a)). Based on Section 1.2, we choose the triangular honeycomb composed of six springs and a dodecagonal mass block as the unit cell. Considering the difficulty and cost of potential material fabrication, the lattice constant of the unit cell is set to be a = 18 mm. Each spring has length $h_s = 6$ mm and width $h_d = 0.9$ mm. Given the material properties of the continuum and the relevant dimensions, the spring's Young's modulus is determined by Eq. (6). Meanwhile, according to the theory in Section 1.2, both the stiffness and density of the mass blocks need to be relatively high compared to the springs. Considering existing materials that can be easily manufactured, we choose the PET (Polyester) and stainless steel (Table 1) as the materials to construct the springs and mass blocks, respectively. Afterwards, the mass equivalence with the continuum (Eq. (13)) can be achieved by adjusting the thickness of the stainless steel or by adding some counterweights. It should be mentioned that the design requires the mass block to be constrained with slide rails or torsion springs, such that the in-plane translation is allowed while rotation is inhibited (Xu et al., 2020).

2.2. Arbitrary elastic wave steering

2.2.1. Lattice-based polar solids for wavelength magnification and beam translation

To realize arbitrary waveguiding, we start by dealing with two fundamental wave ray manipulations: wavelength magnification and beam translation. The wave magnification can be obtained by performing a uniaxial stretch transformation Eq. (17) with $\xi_1 = \sqrt{3}$, $\xi_2 = 1$, and $\eta = 0$ on the initial polar solid, where the stiffness of vertical springs stays the same and the horizontal distance of the other four springs increases with their stiffness and orientation unchanged. With the weight of the mass blocks unchanged, its width is then adjusted accordingly to ensure the structural connectivity. Next, we increase its height to reduce the bending stiffness so that we can avoid unnecessary elastic deformation during wave propagation. Furthermore, the length and width of the two vertical springs are adjusted (proportionally reduce the size of the spring) to keep the stiffness unchanged. Fig. 2(b) demonstrates the unit cell microstructure of the polar solid for wavelength magnification. Following a similar principle and approach, the polar solid for the beam translation can be designed with its microstructure shown in Fig. 2(c). We use the same two types of springs employed in uniaxial stretched polar solid. The springs on the left and right sides of the transformed polar lattice are sheared by a distance of ηd with $\eta = 1/\sqrt{3}$ and the width of the waveguide being d. The connection of the springs is ensured by adjusting the

shape of the mass block. The deformed unit cell is also inserted in Fig. 2(c). Therefore, the proposed microstructures could provide meaningful guidance for experimental demonstration and validation in the future.

In this study, dispersion relations are utilized to examine the elastodynamic equivalence between the continuum (host medium) and the polar lattices before and after the global transformations, and to determine the operation frequency band of the designed media. In the numerical simulations, the Bloch-Floquet conditions is applied for the continuum (not shown), the initial polar lattice, and the sheared and stretched polar lattices (Figs. 2(a)–(c)). The dispersion relations are subsequently obtained by eigenvalue analysis utilizing the solid-mechanics module of COMSOL Multiphysics. Fig. 2(d) displays the dispersion curves of the four media in the Γ -M directions of the first irreducible Brillouin zones. It is also worth to mention that the dynamic performance of the transformed lattices (stretched and sheared) is almost the same as that of the initial lattice. It is clearly illustrated that the P and S wave branches of the four media match well in 0–14 kHz and 0–10.5 kHz, respectively. Therefore, the wave frequency range (0–10.5 kHz) is considered as the operation frequency range where the spatial equivalence holds for elastic wave steering. Moreover, it is important to provide deep understanding of work mechanisms to break the spatial equivalence in dynamic range, which will be leveraged to perform agile wave propagation analysis and future microstructural design optimization. From Fig. 2(d), it can be easily noticed that the P and S wave bandgaps caused by the local resonances and Bragg scattering in the lattice near 18 kHz and 13 kHz, respectively, are main factors to break the spatial equivalence between the continuum medium and initial, stretched and sheared polar lattices in dynamic range. A simple and feasible solution to enhance the dynamic range of spatial equivalence is to reduce the size of the unit cell with acceptable manufacturing accuracy and cost.

Two fundamental waveguides are then numerically demonstrated by the proposed lattice-based polar solids. Fig. 3 shows full-scale simulation results of P (13 kHz) or S (6 kHz) Gaussian beam propagating in a continuum medium embedded with the initial (Figs. 3(c)–(d)) and transformed polar solids (Figs. 3(e)–(f)) of 7 × 40 unit cells and Figs. 3(g)–(h) of 13 × 36 unit cells using the frequency domain analysis. Perfectly matched layers (PMLs) are built around the medium to eliminate any unwanted boundary reflections. Compared with the reference cases (Figs. 3(a) and (b)) for the P and S waves propagating on continuum medium, part of the continuum is discretized into the lattice structure in Fig. 3(c) and (d). Neither significant wave reflection nor amplitude reduction of the wave transmission is observed to validate an excellent spatial equivalence between the continuum and the initial lattice. The P and S wave propagation in the stretched lattices and shear lattices can be found in Figs. 3(e)–(h). Note that the waves in Fig. 3(c) and (d) have identical wavelengths λ_0 as those in the continuum, whereas the wavelengths indicated in Fig. 3(e) and (f) are magnified by a factor of $\xi_1 = \sqrt{3}$. Meanwhile, the simple sheared polar lattice (Figs. 3(g) and (h)) shift the wave beams upward by ηd , where $\eta = 1/\sqrt{3}$ and the width of the waveguide $d = 13\sqrt{3}a/2$. Although the transformed polar lattices occupy different physical spaces, the transmitted waves can fully recover to the incident P and S waves profile, thus illustrating its ability of wave ray steering.

2.2.2. Lattice-based polar solid for extreme wave steering

Informed by the local affine transformation and the global transformed lattice, we now explore ways to design an extreme waveguide with a steering angle $\beta = 90^{\circ}$ as shown in Fig. 4(a). Specifically, we rotate each vertical row of mass blocks of the uniaxial stretched polar lattice Fig. 2(b) by 3° around the neutral line from left to right. Subsequently, the lengths of the mass blocks are adjusted accordingly from the inside to the outside of the sector to compensate the change in the size of the unit cells due to rotation. Meanwhile, the length and stiffness of the springs are unchanged. As a result, the connection of the mass array deviates in the relative positions between the springs and the mass block in each unit cell with respect to that before the bending. However, it can be expected that such a small adjustment will not affect the spatial equivalence of the transformed lattices because it is much smaller than the operation wavelength. A polar lattice constructed for the extreme wave bent is shown in Fig. 4(a). It is worth noting that the vertical position of the neutral line in the bending waveguide can be adjusted arbitrarily, and its elaborate selection can make the inner boundary of the bending waveguide with the same length as the lower boundary of the initial lattice. Under this context, the initial lattice and the bending waveguide will maintain the same mass block size at the corresponding positions on both boundaries, which is of practical importance for the realization of the design.

The performance of the transformed polar lattices in steering the P and S waves is numerically examined in Fig. 4(b) and (c). Similarly, Gaussian wave beams of P and S waves (with the frequencies 12 kHz and 6 kHz, and the beam widths 300 mm and 400 mm, respectively) are horizontally impinging on the waveguide. It clearly illustrates that both beams have been perfectly bent 90° without any waveform distortion or energy loss. Fig. 4(d) displays the transmission spectrum of the polar lattices for P and S waves. Here, the transmittance is defined as W_{out}/W_{in} with

$$W_{out,in} = \int \rho \omega^2 (u_1^2 + u_2^2)/4 \ ds_{out,in}$$
 (18)

where u_1 and u_2 are the displacement components, ω is the angular frequency and $s_{out,in}$ refers to the corresponding integration regions shown in Fig. 4(b). The high transmission within the operation frequency ranges validates that the small adjustment does not affect the waveguide performance. Perfect P and S wave bending is observed when the operation wave is lower than the space equivalence frequency limits (14 kHz for the P wave and 10.5 kHz for the S wave). Surprisingly, waveguide performs less effectively at low frequency range (smaller than 3 kHz), which is mainly caused by the limitation of the finite beam width. It is also worth noting that, beyond the operation frequency range, the waveguide's performance of bending S wave is poor compared to that of P wave. P wave maintains a relatively high transmission while transmission of S wave almost drops to zero.

Having abilities for wave steering and shifting, we now further demonstrate the elastic wave control in an arbitrary manner where the sheared and stretched polar lattices will be mixed. Fig. 5 illustrated an arbitrary wave steering for both P and S waves

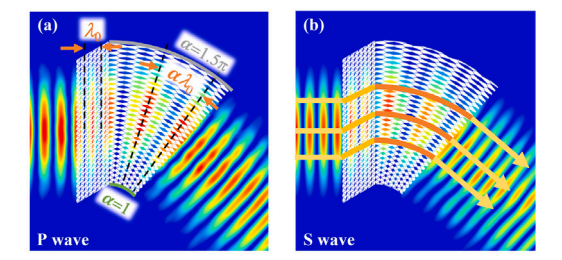


Fig. 5. Numerical simulations for an arbitrary body waveguide. (a-b) Simulation for total displacement fields of horizontal (a) P wave (10 kHz), and (b) S wave (6 kHz) beams propagation through the waveguide.

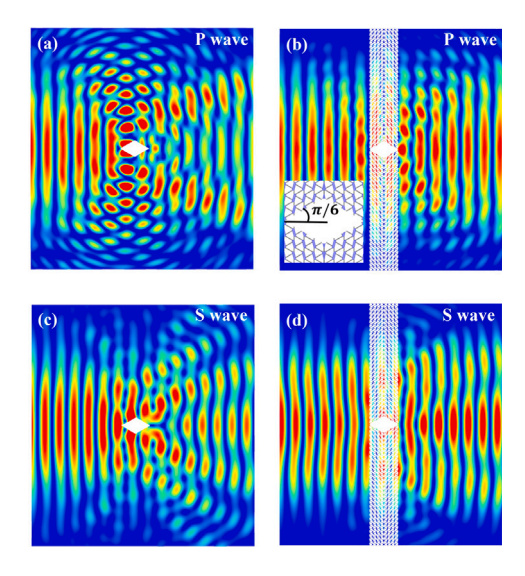


Fig. 6. Numerical simulations of the unidirectional cloaking. The cloak comprises four simple-sheared polar solids, as proposed in Section 2.2.1, and each block consists of 4×30 cells. (a-b) Simulation for P wave at 9 kHz (a) with or (b) without unidirectional cloaking device. (c-d) Simulation for S wave at 5 kHz (c) with or (d) without unidirectional cloaking device. The zoomed in view in (b) shows the defects and the microstructures.

at 10 kHz and 6 kHz, respectively. In the example, the simple-sheared polar lattice consists of 8×30 cells with a 4a shift and the stretched lattice under affine transformation consists of 7×30 cells with a 42° bending is assembled. The orientation and the angle of the wave beam are modulated with the shift distance and the bending angle of two transformed polar lattices, respectively. The perfect material impedance match between the two transformed lattices guarantees the almost perfect wave steering along any arbitrary direction.

2.2.3. Unidirectional cloaking

The need to protect or cloak objects against unwanted mechanical vibration and wave incidence is a long-standing subject in engineering, especially for objects with arbitrary shapes. The main obstacle is the form-invariance under the elastic transformation theory. In this section, we demonstrate the unidirectional cloaking, the stealth of a diamond-shaped object, by simply using sheared lattice-based polar solids. To suppress elastic wave scattering from a diamond-shaped void defect with inclined angle $\pi/6$ (Fig. 6(a)), the unidirectional cloaking medium (Fig. 6(b)) can be constructed by combining four lattice-based sheared polar solids (each consisting of 4 × 30 unit cells). As shown in Fig. 6(a) and (c), the diamond-shaped void defect induced significant scattering effect form the incident Gaussian elastic wave beams of P-mode at 9 kHz and S-mode at 5 kHz. The cloaking performance is assessed based on the transmitted wave field over the constructed lattice-based polar medium. The results demonstrate overall a satisfactory cloaking performance for both P and S waves. The performance for the S wave mode is expected to worse than the P wave mode because the probing wavelength for the S wave mode is closer to the lattice parameter used.

3. Rayleigh surface wave cloaking on curved polar surfaces

Rayleigh waves propagate along surfaces with their fields confined to the neighborhoods of the surfaces. Recently, Rayleigh waves have found application in the ultrasonic nondestructive evaluation of structures with curved surfaces (Zhang et al., 2020b). However, the velocity of the surface wave increases with greater concave surface curvature, and a Rayleigh wave no longer exists

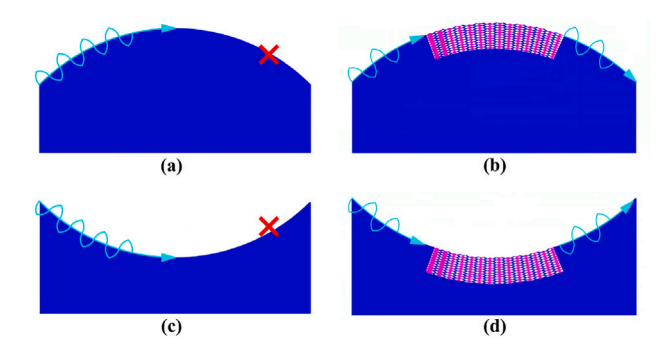


Fig. 7. Schematic of proposed polar lattice as Rayleigh waveguide. (a-b) Rayleigh waves propagating on convex surfaces (a) without and (b) with polar lattices. (c-d) Rayleigh waves propagating on concave surfaces (c) without and (d) with polar lattices.

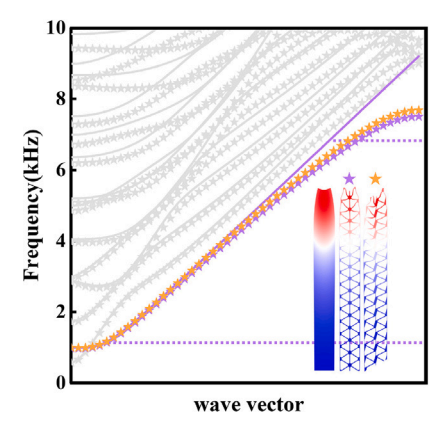


Fig. 8. Dispersion relations of the continuum and the lattice-based polar solids for a horizontally infinite and vertically bounded (with the free top boundary and fixed bottom boundary) domain. The branches of the Rayleigh wave mode of the continuum and the polar solids are highlighted.

once the surface wave velocity exceeds the bulk shear wave velocity. Moreover, the energy in the Rayleigh wave is transferred to other modes and cannot propagate on convex surfaces with large curvature (Rulf, 1969; Harris, 2002; Zhang et al., 2020b). Unlike in these domains where research has advanced to elastic and acoustic wave cloaking, little to no work succeeded in probing the problem of Rayleigh wave cloaking on curved surfaces with excessive curvatures (Fig. 7). In the study, the lattice-based polar solids are suggested to break this fundamental limitation by leveraging their spatial equivalence and enable the Rayleigh wave cloaking on curved surfaces with excessive curvatures as if it propagates in the flat free surface. On the other hand, these polar lattices can be adversely used for wave mitigation on curved surfaces in their bandgap frequencies because of the microstructure effects.

3.1. Rayleigh wave validation in the half-space polar lattice

Before applying the polar lattice for Rayleigh wave cloaking, the spatial equivalence of the half-space continuum medium and the half-space transformed polar lattices is validated first by means of surface wave dispersion comparison. Three supercells of 2×15 unit cells of a continuum and the corresponding initial (Fig. 2(a)) and sheared lattices (Fig. 2(c)) of the same size are constructed with their top free boundaries, the fixed bottom boundary, and left and right boundaries being Bloch-Floquet periodicity. Their dispersion curves for the Bloch wave in the horizontal direction are shown in Fig. 8 with the branches of the Rayleigh wave modes highlighted. It is noted that the spatial equivalence between the lattice structure and continuum medium on the Rayleigh surface wave modes is observed for the frequency from 1.4 kHz to 7 kHz. The lower bound of the operation frequency being at 1.4 kHz instead of zero frequency is induced by the finite thickness of the selected media in the numerical simulation.

3.2. Rayleigh wave cloaking and mitigation on curved polar surfaces

With the proposed polar lattices, we are ready to construct a curved cloak for Rayleigh waves. Fig. 9 shows the wave field simulation of the transformed polar lattice for Rayleigh surface wave propagation. In the study, the transformed lattice is formulated by the same one in the wave bent simulation. A U-shaped domain is connected by the lattice-based polar solid at its center right and perfectly matched layers arranged at both ends. The point sources are indicated by the red arrows. When the point source at 5 kHz is excited at the midpoint of the upper boundary of the continuum domain, the Rayleigh wave is unable to propagate

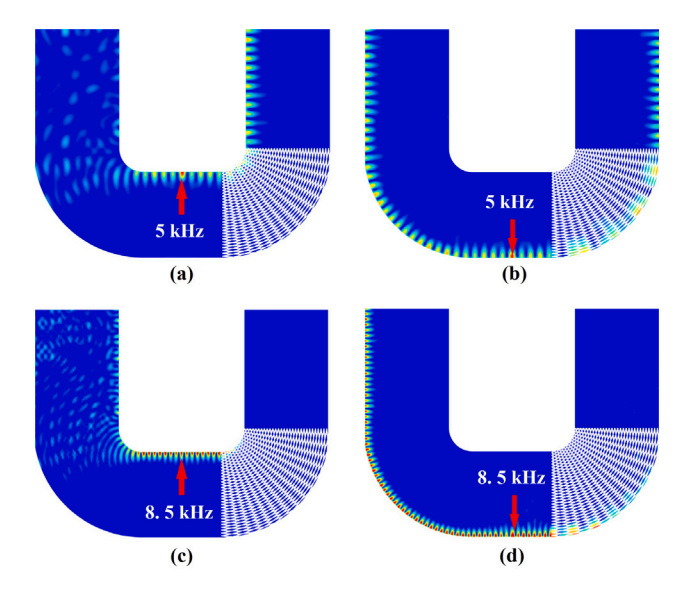


Fig. 9. Numerical simulations of Rayleigh surface wave cloak by using transformed polar lattices. (a-d) Simulations for surface wave excitation (a-b) at 5 kHz, which is within polar lattices' operation frequency and (c-d) at 8.5 kHz, which is within band gap. The wave source is located at the concave or convex surface of a U-shaped domain with the designed bending waveguide at its right corner.

through the left sharp concave surface but penetrates into the bulk (Fig. 9(a)), indicating that the concave surface indeed hinders the Rayleigh wave propagation to the left. However, thanks to the spatial equivalence of the lattice-based polar solid, the Rayleigh wave passes perfectly through the concave surface on the right-hand side as it propagates on the flat free surface. Fig. 9(b) illustrates that the Rayleigh wave can smoothly propagate in both continuum and lattice-based polar media on the convex surfaces with large curvature. The numerical simulation validates the performance of the lattice-based polar solid in manipulating the Rayleigh surface wave propagation on curved surfaces with large curvature. By comparison of waves propagating in the left and right directions, it shown that the wavelength is magnified in the lattice-based polar solid, but no energy leak is observed. On the other hand, Figs. 9(c) and (d) demonstrate the filtering effect on the Rayleigh wave of 8.5 kHz, which is within the bandgap of the lattice-based polar solid. The wave propagation is prohibited for both concave and convex surfaces in polar lattice at this frequency. However, in the continuum medium, the Rayleigh wave propagation along concave surface with large curvature and convex surface with small curvature displays opposite effects, which are expected.

As illustrated in Fig. 8, the sheared lattice-based polar solid have the identical Rayleigh wave modulation capability in the same frequency range as the stretched lattice-based polar solids. To validate this capability, its performance for Rayleigh wave guiding and filtering on both concave and convex sheared surfaces are illustrated in Fig. 10 for both 5 kHz and 8.5 kHz. As shown in Fig. 10(a-d), sheared surfaces with concavity and convexity significantly affect the propagation of the Rayleigh wave in the continuum medium, where the large wave diffraction is evidenced on the curved surface. At 5 kHz, significant portions of Rayleigh wave dissipate into the bulk for both concave and convex surfaces as in Fig. 10(a) and (b), respectively. Similar phenomenon can be found for Rayleigh wave at 8.5 kHz, as shown in Fig. 10(c-d). Meanwhile, with perfect phase match comparing with continuum medium, designed polar lattices can perfectly guide the Rayleigh wave propagation on both concave and convex surfaces, see Fig. 10(a-b). Fig. 10(c-d) shows the numerical simulation results for Rayleigh wave at 8.5 kHz. The sheared lattice-based polar solid clearly failed to redirect the Rayleigh wave due to the bandgap, see Fig. 8. Its frequency dependence (dispersion) from the physical properties of the polar medium adjacent to the surface and the surface could be improved by conducting microstructure optimization, which will be investigated in the near future.

3.3. Arbitrary curved surface waveguiding

There is always of practical significance to smoothly guide Rayleigh wave propagation on arbitrary curved surfaces such as earthquake mitigation. To accomplish this goal, the sheared and stretched lattice-based polar solids are assembled to form an arbitrary curved surface, as shown in Fig. 11. Because Rayleigh wave will be exponentially decayed along the perpendicular surface direction, the thickness of the waveguide only needs to be greater than 20% of the attenuation depth of the Rayleigh wave. Considering this fact, an arbitrary waveguide consisting of lattice-based sheared and stretched polar solids is constructed in a shifting-bending-shifting path control paradigm with the number of cells 8×6 , 7×6 , and 8×6 , respectively. As shown in Fig. 11(a), Rayleigh wave at frequency 6.5 kHz can propagate smoothly on the first convex surface section and diffract into the bulk when it encounters the concave surface section in the continuum medium. As expected, the proposed lattice-based polar surface can successfully transport the Rayleigh wave through the arbitrary curved surface with very little energy loss (Fig. 11(b)).

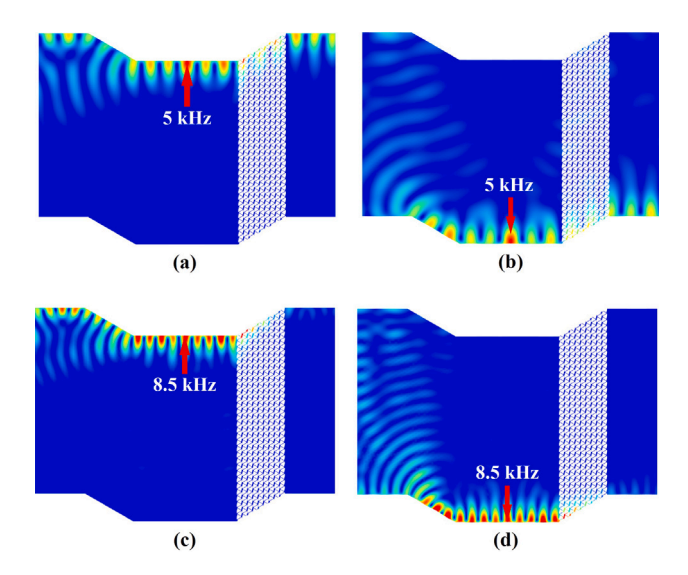


Fig. 10. Numerical simulations of the simple-sheared polar solid for Rayleigh surface wave mode. (a-d) Simulations for surface wave excitation (a-b) at 5 kHz, which is within polar lattices' operation frequency and (c-d) at 8.5 kHz, which is within band gap. The wave source is located at the top and bottom surfaces of an armchair domain with the designed shear waveguide at its center right.

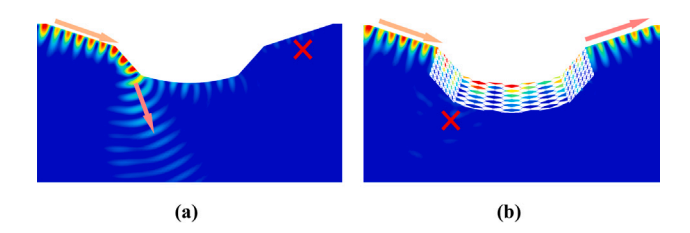


Fig. 11. Numerical simulation of Rayleigh wave at 6.5 kHz. (a) the case without the waveguide and (b) an arbitrary waveguide with finite thickness.

4. Conclusion and discussion

In summary, we report and validate a microstructure design paradigm based on discrete transformation elasticity to realize inhomogeneous lattice-based polar medium that can serve as perfect waveguide for both elastic P and S waves. In the proposed strategy, we construct the lattice-based polar medium based on discrete transformation elasticity (DTE). The discretized lattice is further engineered for wave magnification, wave translation and steering by using global linear transformation and local affine transformation. The underlying principle is based on an established equivalence between geometric discrete transformations acting on different wave paths and material transformations acting on the constitutive properties. In this way, the present work establishes the first theoretical and numerical evidence of the lattice-based polar medium in full plane wave control thanks to the lattice-based polar metamaterials. The inhomogeneous lattice-based polar medium is then leveraged for Rayleigh wave control on curved surfaces to break the conventional limit of Rayleigh wave propagation on the concave and convex surfaces with large curvature. The designed polar solids and waveguides provide a feasible paradigm for implementing DTE and its engineering applications.

Hopefully, this study will enlighten future research in the same realm. In addition to the preparation and experimental validation of the proposed device, the development of polar solids for anisotropic host media has a promising application prospect. Although there are no theoretical obstacles, the design and development of 3D polar solids, which are more complex than the 2D ones, still require further design and investigation. Furthermore, it would be interesting to explore deformable polar solids that are tunable or smart (Shin et al., 2012). A comprehensive investigation is needed of the associated deformation mechanisms, as well as their influences on the elastodynamic behavior.

CRediT authorship contribution statement

Shiheng Zhao: Formal analysis, Performing simulations, Writing. Jiaji Chen: Performing simulations, Writing. Zheng Chang: Conceptualization, Validation, Supervision, Funding acquisition, Writing. Guoliang Huang: Conceptualization, Validation, Supervision, Funding acquisition, Writing.

Declaration of competing interest

The authors declare that they have no known competing financial interests or personal relationships that could have appeared to influence the work reported in this paper.

Data availability

Data will be made available on request.

Acknowledgments

G.L.H. thanks the financial support from the NSF CMMI under Award No. 1930873, the U.S. Air Force Office of Scientific Research (grant no. AF 9550-20-0279) under Program Manager Dr. Byung-Lip (Les) Lee and the Army Research Office, USA under Grant No. W911NF-18-1-0031 with Program Manager Dr. Daniel Cole. Z.C. thanks the fund support from the National Natural Science Foundation of China (Grant No. 11602294) and the 2115 Talent Development Program of China Agricultural University.

References

Ashby, M., 2008. Teaching engineering materials: the ces edupack. In: Granta's, C. (Ed.), CES EduPack Database of Natural and Man-Made Materials. Cambridge, UK. np. 1–13.

Brun, M., Guenneau, S., Movchan, A.B., 2009. Achieving control of in-plane elastic waves. Appl. Phys. Lett. 94 (6), 061903.

Bückmann, T., Kadic, M., Schittny, R., Wegener, M., 2015. Mechanical cloak design by direct lattice transformation. Proc. Natl. Acad. Sci. 112 (16), 4930–4934.

Chang, Z., Guo, D., Feng, X.-Q., Hu, G., 2014a. A facile method to realize perfectly matched layers for elastic waves. Wave Motion 51 (7), 1170-1178.

Chang, Z., Guo, H.-Y., Li, B., Feng, X.-Q., 2015. Disentangling longitudinal and shear elastic waves by neo-Hookean soft devices. Appl. Phys. Lett. 106 (16), 161903.

Chang, Z., Hu, J., Hu, G.-K., 2010. Transformation method and wave control. Acta Mech. Sinica 26 (6), 889-898.

Chang, Z., Hu, J., Hu, G., Tao, R., Wang, Y., 2011. Controlling elastic waves with isotropic materials. Appl. Phys. Lett. 98 (12), 121904.

Chang, Z., Liu, X., Hu, G., 2014b. Heat flow control by transformation method with grid generation method. Acta Mech. Solida Sin. 27 (5), 454-460.

Chen, H., Chan, C.T., Sheng, P., 2010. Transformation optics and metamaterials. Nature Mater. 9 (5), 387-396.

Chen, Y., Nassar, H., Huang, G., 2021. Discrete transformation elasticity: An approach to design lattice-based polar metamaterials. Internat. J. Engrg. Sci. 168, 103562.

Cummer, S.A., Schurig, D., 2007. One path to acoustic cloaking. New J. Phys. 9 (3), 45.

Forte, S., Vianello, M., 1997. Symmetry classes and harmonic decomposition for photoelasticity tensors. Internat. J. Engrg. Sci. 35 (14), 1317-1326.

Gokhale, N.H., Cipolla, J.L., Norris, A.N., 2012. Special transformations for pentamode acoustic cloaking. J. Acoust. Soc. Am. 132 (4), 2932-2941.

Harris, J.G., 2002. Rayleigh wave propagation in curved waveguides. Wave Motion 36 (4), 425-441.

Hu, J., Chang, Z., Hu, G., 2011. Approximate method for controlling solid elastic waves by transformation media. Phys. Rev. B 84 (20), 201101.

Kadic, M., Bückmann, T., Schittny, R., Wegener, M., 2015. Experiments on cloaking in optics, thermodynamics and mechanics. Phil. Trans. R. Soc. A 373 (2049), 20140357.

Meirbekova, B., Brun, M., 2020. Control of elastic shear waves by periodic geometric transformation: cloaking, high reflectivity and anomalous resonances. J. Mech. Phys. Solids 137, 103816.

Milton, G.W., Briane, M., Willis, J.R., 2006. On cloaking for elasticity and physical equations with a transformation invariant form. New J. Phys. 8 (10), 248. Nassar, H., Chen, Y., Huang, G., 2018. A degenerate polar lattice for cloaking in full two-dimensional elastodynamics and statics. Proc. R. Soc. Lond. Ser. A Math. Phys. Eng. Sci. 474 (2219), 20180523.

Nassar, H., Chen, Y., Huang, G., 2019. Isotropic polar solids for conformal transformation elasticity and cloaking. J. Mech. Phys. Solids 129, 229-243.

Nassar, H., Chen, Y., Huang, G., 2020, Polar metamaterials: a new outlook on resonance for cloaking applications, Phys. Rev. Lett. 124 (8), 084301.

Norris, A.N., 2008. Acoustic cloaking theory. Proc. R. Soc. A 464 (2097), 2411-2434.

Norris, A.N., Parnell, W.J., 2012. Hyperelastic cloaking theory: transformation elasticity with pre-stressed solids. Proc. R. Soc. A 468 (2146), 2881–2903.

Norris, A.N., Shuvalov, A.L., 2011. Elastic cloaking theory. Wave Motion 48 (6), 525-538.

Pendry, J.B., Schurig, D., Smith, D.R., 2006. Controlling electromagnetic fields. Science 312 (5781), 1780-1782.

Phani, A.S., Woodhouse, J., Fleck, N., 2006. Wave propagation in two-dimensional periodic lattices. J. Acoust. Soc. Am. 119 (4), 1995-2005.

Rulf, B., 1969. Rayleigh waves on curved surfaces. J. Acoust. Soc. Am. 45 (2), 493-499.

Schittny, R., Kadic, M., Guenneau, S., Wegener, M., 2013. Experiments on transformation thermodynamics: molding the flow of heat. Phys. Rev. Lett. 110 (19), 195901.

Schurig, D., Mock, J.J., Justice, B., Cummer, S.A., Pendry, J.B., Starr, A.F., Smith, D.R., 2006. Metamaterial electromagnetic cloak at microwave frequencies. Science 314 (5801), 977–980.

Shin, D., Urzhumov, Y., Jung, Y., Kang, G., Baek, S., Choi, M., Park, H., Kim, K., Smith, D.R., 2012. Broadband electromagnetic cloaking with smart metamaterials. Nature Commun. 3 (1), 1–8.

Willis, J.R., 1981. Variational principles for dynamic problems for inhomogeneous elastic media. Wave Motion 3 (1), 1-11.

Wu, Q., Huang, G., 2022. Omnidirectional wave polarization manipulation in isotropic polar solids. Int. J. Solids Struct. 241, 111481.

Xu, X., Wang, C., Shou, W., Du, Z., Chen, Y., Li, B., Matusik, W., Hussein, N., Huang, G., 2020. Physical realization of elastic cloaking with a polar material. Phys. Rev. Lett. 124 (11), 114301.

Zhang, H., Chen, Y., Liu, X., Hu, G., 2020a. An asymmetric elastic metamaterial model for elastic wave cloaking. J. Mech. Phys. Solids 135, 103796.

Zhang, S., Qin, L., Li, X., Kube, C.M., 2020b. Propagation of Rayleigh waves on curved surfaces. Wave Motion 94, 102517.

Zhang, S., Xia, C., Fang, N., 2011. Broadband acoustic cloak for ultrasound waves. Phys. Rev. Lett. 106 (2), 024301.